Reports

Microearthquake Imaging of the Parkfield Asperity

P. E. MALIN, S. N. BLAKESLEE, M. G. ALVAREZ, A. J. MARTIN

Microearthquake data from a downhole seismometer network on the San Andreas fault appear to outline two aseismic asperities that may correspond to the locations of the foreshocks and main shocks of the Parkfield characteristic earthquakes. The source parameters of the microearthquakes show that a few of the earthquakes have significantly higher stress drops than most. Furthermore, the magnitude-frequency statistics suggest that at local magnitude 0.6, the cumulative number of small events begins to fall off the usual Gutenberg-Richter ($b = -1$) relation, in which the number of events increases exponentially with decreasing magnitude. The downhole seismometer data establish a baseline from which the evolution of the earthquake process at Parkfield can be monitored and suggest that different mechanical conditions than those that lead to the typical Gutenberg-Richter relation may be operating for the smallest of Parkfield microearthquakes.

BY STUDYING A RESTRICTED SEGMENT of the San Andreas fault near Parkfield, California, we have obtained a catalogue of microearthquakes that is complete to roughly local magnitude 0. The detection and recording of these microearthquakes was accomplished on a ten-station network of downhole seismometers, which we call the Parkfield Downhole Digital Seismic Network (DDSN) (*1–3*). The stations of the DDSN are located more or less in a circle around the epicenter of the 1966 Parkfield characteristic earthquakes (Fig. 1) (*4*). Understanding the seismicity of this location is important because the National Earthquake Prediction Advisory Council has accepted a prediction for a magnitude 5.5 to 6.0 earthquake there within the next 4 years (*5*).

Although some aspects of the spatial distribution and stress drops of Parkfield microearthquakes have been observed with other networks (*6–10*), the lowered detection threshold, low background noise, and high dynamic range of the DDSN data provide more complete coverage while corroborating the findings based on less sensitive equipment. A total of 538 Parkfield microearthquakes were recorded between 30 June 1987 and 5 January 1989. For each event, we catalogued the origin time and location, the difference in P- and S-wave travel times, the seismic moment, and the corner frequency at which the displacement spectrum began to roll off as observed at the Vineyard Canyon (VC) station. The moments and corner frequencies were used to calculate equivalent local duration magnitudes and Brune stress drops (*11–14*).

The locations of the events show that there are prominent gaps in the distribution of epicenters near the Middle Mountain (MM) and Eades (ED) stations (Fig. 1). There are also seismically quiet patches in the distribution of the along-fault hypocenters north and south of the Middle Mountain epicenter gap (Fig. 2). The event epicenters are considerably more scattered outside the perimeter of the locating network than inside it. The southward fanning of epicenters to the northwest of Stockdale Mountain (ST) station and with depth is most likely a product of location errors resulting from the presence of higher-velocity rock to the west of the San Andreas fault than to the east (*7*). The relative magnitudes of the microearthquakes are not strongly correlated to corner frequency (Fig. 3A). Nor are the calculated magnitudes or corner frequencies affected by event depth (Fig. 3, B and C). However, the events with the largest moments tend to have a limited range of corner frequencies and depths (Fig. 3, D and E). Combination of the corner frequencies and moments to obtain the stress drops shows that the events with the largest stress drops tend to cluster around two depth horizons on the fault, one centered at 4 km, the other at 10 km (Fig. 3F).

Occurrence of high-stress-drop events at a depth of 10 km near the hypocenter of the 1966 Parkfield earthquake has been recognized previously in studies of time-domain waveforms; in our study, we used frequency domain methods (*8*). The locations of our high-stress-drop events tend to cluster near the edges of the aseismic patches described above (*15*). The smallest microearthquake captured by the DDSN is a relative magnitude -0.73 event at a depth of 5 km southeast of the MM station. On the basis of the data in Fig. 3B, the coverage of the DDSN on the limited fault segment at Parkfield is complete for events less than 12 km deep with magnitudes greater than 0.

The magnitude-frequency (Gutenberg-Richter) statistics of the events located on the San Andreas fault fall considerably off the usual $b = -1$ slope for magnitudes less than approximately 0.6 (Fig. 4). At magnitude 0, the full data set has only about half the cumulative number of earthquakes predicted by the $b = -1$ Gutenberg-Richter relationship. To make sure that this roll-off is not simply a product of the detection limit of the DDSN, we have calculated the statistics for three subsets of data: one that is

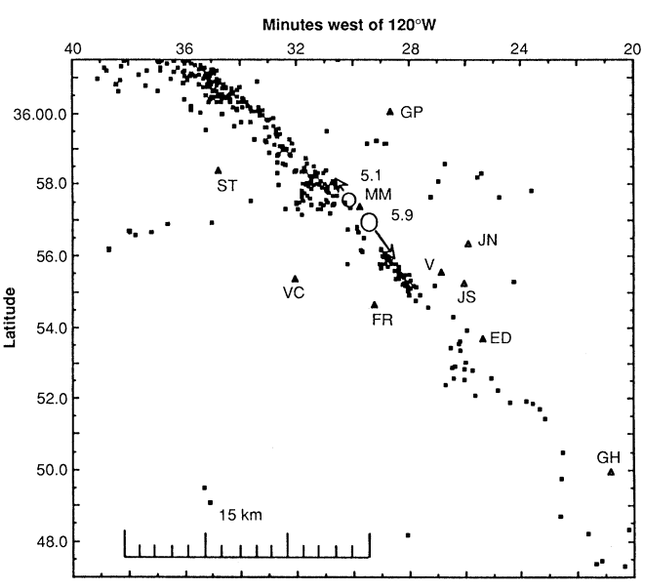

Fig. 1. The locations of the DDSN stations (triangles) and the epicenters of the microearthquakes detected from 30 June 1987 to 5 January 1989 (boxes). Epicenters of the magnitude 5.1 foreshock and 5.9 main shock [respectively north and south of the Middle Mountain (MM) station] of the 1966 Parkfield characteristic earthquake are shown by open circles with arrows that point in their rupture directions (*4, 7*). Other station names are: ED, Eades; FR, Frolich; GH, Gold Hill; GP, Gastro Peak; JN, Joaquin North; JS, Joaquin South; ST, Stockdale Mountain; V, Varian; VC, Vineyard Canyon.

Institute for Crustal Studies, University of California, Santa Barbara, CA 93106.

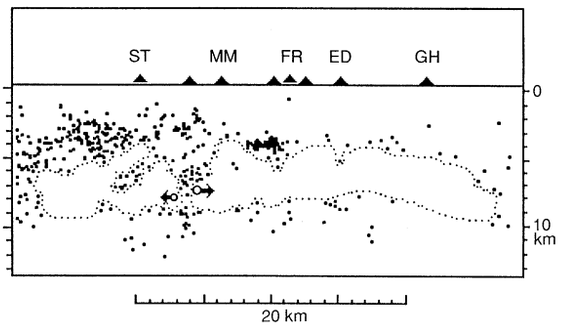

Fig. 2. Cross-sectional view with the microearthquake hypocenters projected onto a plane parallel to the San Andreas fault. The DDSN stations are shown by triangles. The hypocenters and rupture directions of the largest foreshock and the main shock of the 1966 Parkfield characteristics are shown by open circles with arrows pointing in the direction of their rupture. The aseismic patches that we identify with the asperities of the 1966 main shock and largest foreshock are outlined by dotted lines.

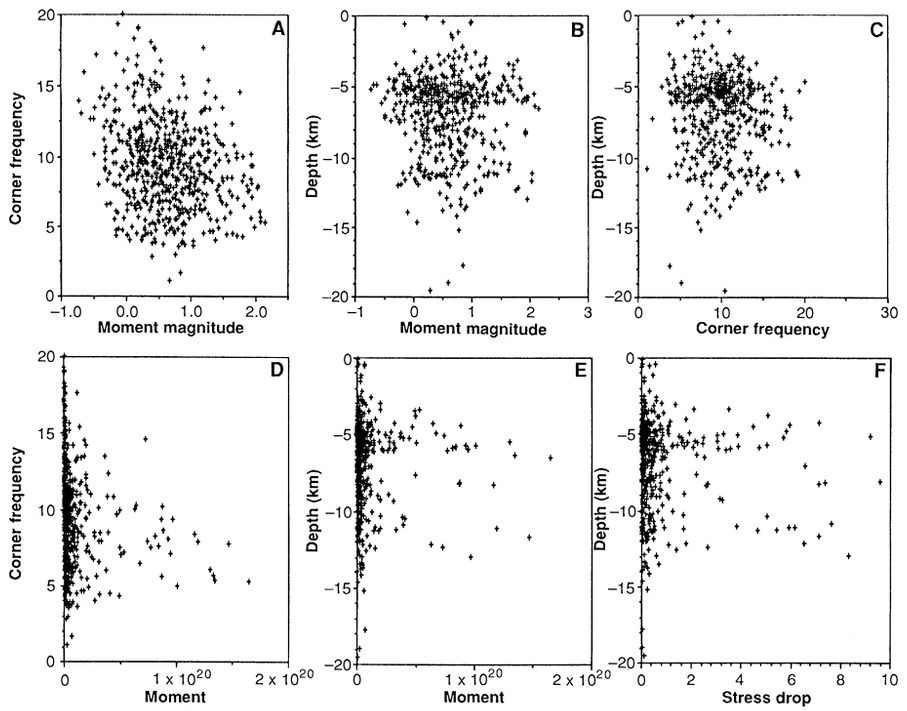

Fig. 3. The distribution of various source parameters for Parkfield microearthquakes. (**A**) Corner frequency versus relative magnitude; the magnitudes were determined from the moment of each event; only the S-waves at the VC station were used in calculating the moments and corner frequencies. (**B**) The depth distribution of different magnitude events. Based on this figure, the magnitude-depth detection threshold of the DDSN is at $M_{USGS} = 0$ at a depth of 12 km. (**C**) The depth distribution of event corner frequencies. (**D**) Corner frequency versus moment. (**E**) The depth distribution of event moments. (**F**) The depth distribution of event stress drops.

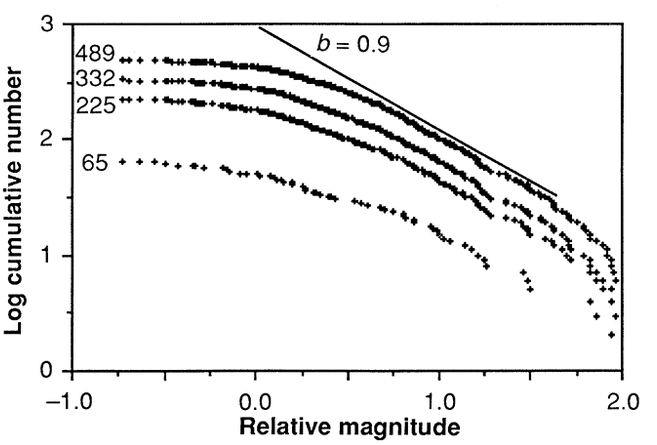

Fig. 4. The cumulative magnitude-frequency statistics for the events located within four progressively smaller patches of the San Andreas fault covered by the DDSN. The number of events in each subset is shown on the left. The largest set contains all the events detected on the main trace of the San Andreas fault. The smallest set contains the events from the cluster nearest the VA station. A b value curve of -0.9, a conservative estimate, is shown for comparison.

complete for all magnitude 0 and larger events, one that is complete for all magnitude -0.25 and larger events, and one that includes only events from a microearthquake cluster near the center of the DDSN at the Varian (V) site. We obtained the first two subsets by plotting the locations of (i) all magnitude 0 and smaller earthquakes and eliminating all events beyond their geographic limits, and (ii) all magnitude -0.25 and smaller earthquakes and eliminating all events beyond their geographic limits. For the third subset, we eliminated all events not in the V cluster, which has the tightest station coverage and from which the smallest detected event came (Figs. 1, 2, and 4). The resulting subsets come from progressively smaller sections of the fault zone near the center of the network. All of these curves fall off the $b = -1$ slope at a magnitude considerably greater than 0. Thus, the standard $b = -1$ relation may not be valid along this section of the San Andreas fault.

The aftershocks of moderate to large earthquakes tend to cluster around the edges of the main event slip zone, which presumably was a strong point on the associated fault (*16, 17*). This observation has led to the suggestion that microearthquake events should cluster around the asperities on which recurring or characteristic earthquakes take place (*17*). If this notion is correct, the two aseismic patches we have observed should constitute the asperities on which the characteristic Parkfield earthquakes take place.

Indeed, the seismically quiet patch between Middle Mountain and Gold Hill corresponds generally to the zone of low creep seen in creep and geodetic data (*18*) and to the strong motion slip plane of the 1966 Parkfield ($M = 5.9$) earthquake (*19*), which began under Middle Mountain and ruptured the San Andreas fault toward the southeast (*4*). The 1966 event was preceded by four smaller foreshocks, all of which appear to have been centered a few kilometers to the north of Middle Mountain (*7*). The largest foreshock ($M = 5.1$) ruptured the fault to the northwest (*4*).

On the basis of opposite first motions as observed at Gold Hill, Lindh and Boore (*7*) proposed that the 1966 foreshocks and main shocks took place on different fault segments that have strikes that are misaligned by 5°, with the northwestward segment rotated counterclockwise with respect to the southeastern segment. We propose that this northern segment corresponds to the aseismic patch north of Middle Mountain. If so, we have identified both the main shock and foreshock asperities at Parkfield (Figs. 1 and 2). Both asperities are outlined not only by the background seismicity but also by a

number of high-stress-drop events that occur on their edges.

Based on our analysis of source parameters, two types of microearthquakes appear to be taking place around the aseismic zones. The most common type is a background seismicity of uniformly distributed low-stress-drop (<1 bar) events. Less common are higher-stress-drop (1 to 10 bars) events, which tend to cluster around the asperities. Perhaps these less common events represent the transition between weak and strong parts of the fault zone.

We propose that this character of the microearthquakes is related to the locking up of the San Andreas fault in this region. Our proposal comes from the observation that as events from the creeping fault section northwest of the network are progressively eliminated, the departure from $b = -1$ is progressively larger (Fig. 4). In our model, slip at any point on the fault is a combination of earthquake ruptures and creep, the relative proportion of which might account for the relative numbers of small and large microearthquakes. Perhaps at locations where the fault is strong for longer times and distances, such as at the Parkfield asperities, small displacements are mostly expressed as creep events over large planes. At locations where the fault is easily broken at shorter distance and time scales, small microearthquakes can take place as well as creep, as seems to be happening to the north of Parkfield.

The DDSN catalogue of microseismicity provides a baseline that can be used in monitoring the earthquake process at Parkfield. The evolution of the aseismic zones and high-stress-drop events may provide clues to the mechanics of moderate earthquakes. Likewise, changes in the proportions of smaller microearthquakes, larger microearthquakes, and fault creep may indicate what time- and length-scale factors are controlling slip on this part of the San Andreas fault.

REFERENCES AND NOTES

1. The Parkfield Downhole Digital Seismic Network (DDSN) has been a joint effort between the University of California, Santa Barbara; the University of California, Berkeley; and the U.S. Geological Survey. After prototype downhole stations at Parkfield were tested in 1984 and 1985, construction of the DDSN was begun in 1986 and completed in 1987. Except for the Joaquin South (JS) and Varian (V) sites, all the stations consist of gimbal-leveled three-component, 2-Hz Mark Products L22E seismometers cemented into roughly 75- to 275-m-deep boreholes. At JS, 4.5-Hz phones were installed at 150 m; at V, the phones were installed every few hundred meters to a depth of 1 km.
2. M. Alvarez *et al.*, *Eos* **68**, 1357 (1987).
3. P. Malin, T. McEvilly, T. Moses, *ibid.*, p. 1357 (1987) (abstr.).
4. W. H. Bakun and T. V. McEvilly, *Science* **205**, 1375 (1979).
5. W. H. Bakun and A. G. Lindh, *ibid.* **229**, 619 (1985).
6. J. P. Eaton, M. E. O'Neill, J. N. Murdock, *Bull. Seismol. Soc. Am.* **60**, 1151 (1970).
7. A. G. Lindh and D. M. Boore, *ibid.* **71**, 95 (1981).
8. M. E. O'Neill, *ibid.* **74**, 27 (1984).
9. C. M. Poley *et al.*, *Nature* **327**, 134 (1987).
10. A. J. Michael, *Eos* **69**, 1311 (1988).
11. W. H. Bakun, *ibid.* **74**, 439 (1984).
12. T. Hanks and W. Thatcher, *J. Geophys. Res.* **77**, 4393 (1972).
13. D. J. Andrews, in *Earthquake Source Mechanics*, K. Aki and P. Richards, Eds. (Monograph 37, American Geophysical Union, Washington, DC, 1986), pp. 259–267.
14. After location was determined, the moment and corner frequencies of each event were calculated from the S-wave velocity and displacement power spectra as observed at the VC station (*13*). First, the areas under the above-noise parts of the spectra were calculated by numerical integration. Then, assuming a Brune-type model of the source spectra (*12*), we used the two areas to find the equivalent zero frequency intercept and the characteristic roll-off (corner frequency). With the difference in arrival times between the P- and S-waves at VC and an assumed S-wave velocity of 3.5 km/s, the moment of each event was obtained. The moments of 32 larger events were correlated against their reported California Seismic Network (CALNET) magnitudes, with the result that $M_{USGS} = 0.83 \text{ Log } M_0 - 14.61$ (± 0.2), where M_0 is our calculated moment and M_{USGS} the U.S. Geological Survey established local magnitude scale (*11*); all magnitudes are reported as M_{USGS}.
15. For clarity and brevity the locations of the high-stress-drop events have not been shown explicitly in Figs. 1 and 2 nor in a separate plot. The clustering of the highest stress drops above, below, and to the side of the aseismic patches can be inferred from Fig. 3F.
16. R. S. Cockerham and J. P. Eaton, *U.S. Geol. Surv. Bull.* **1639**, 15 (1987).
17. C. Mendoza and S. H. Hartzell, *Bull Seismol. Soc. Am.* **78**, 1438 (1988).
18. R. Harris and P. Segall, *J. Geophys. Res.* **92**, 7945 (1987).
19. H.-P. Liu, thesis, California Institute of Technology, Pasadena (1983).

20. We thank numerous workers at the University of California, Berkeley, and the U.S. Geological Survey for the data in this report, including T. McEvilly, R. Clymer, D. Lippert, W. Bakun, A. Lindh, W. Ellsworth, A. Record, T. Burdette, B. Dollar, A. Michael, T. Moses, and R. Borcherdt. We thank R. Crosson and M. Woolf for the location software and A. Michael and G. Nishioka for their close cooperation and free scientific exchange during the progress of our work.

14 November 1988; accepted 27 March 1989

Long-Range Electronic Perturbations Caused by Defects Using Scanning Tunneling Microscopy

H. A. MIZES AND J. S. FOSTER

Real-space observations of long-range electronic perturbations caused by defects have been made with scanning tunneling microscopy. The defects are isolated adsorbed molecules on the surface of graphite. These defects perturb the charge density, giving periodic oscillations similar to Friedel oscillations. The oscillations have a wavelength $\sqrt{3}$ times that of the graphite lattice, and the symmetry of the oscillations reflects the nature of the defect.

THE SCANNING TUNNELING MICROscope (STM), an important tool for characterizing solid surfaces with atomic resolution, has recently been used to manipulate and subsequently to observe these surfaces (*1–7*). In this report, we describe and explain peculiarities of the graphite surface that are associated with isolated adsorbed molecules (*8*). Frequently, these adsorbed molecules strongly perturb the surface electronic charge density, giving rise to periodic oscillations that emanate from the defect. These oscillations have the same physical origin as Friedel oscillations, the ripples in the charge density that surround point defects in metals. The images we present here are real-space observations of these oscillations. The oscillations are strikingly apparent in an STM topograph and modulate the graphite lattice with a $\sqrt{3} \times \sqrt{3}$ period. We describe the physical origin of this so-called superlattice in graphite and then show how from the symmetry of the superlattice one can determine the symmetry of the defect itself.

Figure 1 shows two examples of a superlattice effect associated with adsorbed molecules. Figure 1a shows the STM topograph that was obtained after adsorption had been induced by exposure of the graphite to ozone and ultraviolet radiation. In Fig. 1b, the adsorption of a molecular fragment of di(2-ethylhexyl)phthalate was induced by the application of a large voltage pulse to the tip while it was immersed in this liquid (*8*). Both molecules appear as bright spots in the STM topographs, indicating that there is an increased tunneling current when the tip is positioned over the molecule. Far from the adsorbed molecule, the graphite regains its typical hexagonal pattern (*9*). An additional feature, the superlattice, is seen frequently in the intermediate region. It appears that in this region the graphite has undergone a $\sqrt{3} \times \sqrt{3}$ reconstruction. The geometry of this reconstruction depends on the polar

H. A. Mizes, Xerox Webster Research Center, Webster, NY 14580.
J. S. Foster, IBM Research Division, Almaden Research Center, San Jose, CA 95120.